Variability of the Martian thermosphere during eight Martian years as simulated by a ground-to-exosphere global circulation model

Correspondence to:
F. González-Galindo,
ggalindo@iaa.es

F. González-Galindo[1], M. A. López-Valverde[1], F. Forget[2], M. García-Comas[1], E. Millour[2], and L. Montabone[2,3]

[1]Instituto de Astrofísica de Andalucía, CSIC, Granada, Spain, [2]Laboratoire de Météorologie Dynamique, CNRS, Paris, France, [3]Space Science Institute, Boulder, Colorado, USA

Abstract Using a ground-to-exosphere general circulation model for Mars we have simulated the variability of the dayside temperatures at the exobase during eight Martian years (MY, from MY24 to MY31, approximately from 1998 to 2013), taking into account the observed day-to-day solar and dust load variability. We show that the simulated temperatures are in good agreement with the exospheric temperatures derived from Precise Orbit Determination of Mars Global Surveyor. We then study the effects of the solar variability and of two planetary-encircling dust storms on the simulated temperatures. The seasonal effect produced by the large eccentricity of the Martian orbit translates in an aphelion-to-perihelion temperature contrast in every simulated year. However, the magnitude of this seasonal temperature variation is strongly affected by the solar conditions, ranging from 50 K for years corresponding to solar minimum conditions to almost 140 K during the last solar maximum. The 27 day solar rotation cycle is observed on the simulated temperatures at the exobase, with average amplitude of the temperature oscillation of 2.6 K but with a significant interannual variability. These two results highlight the importance of taking into account the solar variability when simulating the Martian upper atmosphere and likely have important implications concerning the atmospheric escape rate. We also show that the global dust storms in MY25 and MY28 have a significant effect on the simulated temperatures. In general, they increase the exospheric temperatures over the low latitude and midlatitude regions and decrease them in the polar regions.

1. Introduction

The Martian thermosphere can be viewed as a transition region between the gravitationally bound lower atmosphere and the exosphere, where molecules and atoms can freely escape from the planet. The thermal and compositional state of the thermosphere has a strong influence over the processes producing atmospheric escape to space. Recent works [*Valeille et al.*, 2009a, 2009b, 2010; *Yagi et al.*, 2012; *Chaufray et al.*, 2015] have shown that local, seasonal, and solar cycle variability of temperature, density, and composition of the thermosphere affect the production and evolution of exospheric species. Therefore, understanding the state of the thermosphere and its variability is of great importance for atmospheric evolution and long-term variability. A coherent reconstruction of the evolutionary history of the Martian atmosphere requires a precise knowledge of the sensitivity of the upper atmosphere to the key parameters driving its variability: the solar flux and the atmospheric dust content. The effect of the variations in the solar output, in the long (young Sun), medium (11 year solar cycle), and short (solar rotation, transitory solar activity) term on the upper atmosphere, has not been sufficiently studied due to the scarcity of data and of modeling efforts.

Most of our observational knowledge of the upper atmosphere of Mars comes from the aerobraking phases of the Mars Global Surveyor (MGS), Mars Odyssey, and Mars Reconnaissance Orbiter spacecraft [*Keating et al.*, 1998, 2009] and the stellar occultation data set obtained by the Spectroscopy for Investigation of Characteristics of the Atmosphere of Mars (SPICAM) instrument on board Mars Express [*Forget et al.*, 2009]. These data sets (and their analysis with computational models) reveal the Martian upper atmosphere to be a complex and dynamically rich region, which can be affected by processes occurring in the lower atmosphere. For example, SPICAM stellar occultations have shown that the presence of a regional dust storm in the lower atmosphere can produce a sudden increase of density in the upper atmosphere [*Forget et al.*, 2009]. It has also been shown

that the interaction of the solar illumination with the prominent Martian topography produces wave structures observed in the thermosphere [*Keating et al.*, 1998]. However, the observational coverage of the upper atmosphere of Mars is significantly less complete than that achieved for the lower and middle atmosphere, for example, with data from the instruments Thermal Emission Spectrometer (TES) on board Mars Global Surveyor [*Smith*, 2004] and Mars Climate Sounder (MCS) on board Mars Reconnaissance Orbiter [*McCleese et al.*, 2010]. Observations during different Martian years (and thus covering a significant fraction of the 11 year solar cycle) with a global spatial coverage are still missing, and so aspects such as the effects of the solar rotation or the solar cycle on the thermosphere are only roughly characterized [*Bougher et al.*, 2015]. Hopefully, the measurements by the Mars Atmosphere and Volatile EvolutioN Mission (MAVEN) spacecraft will fill this gap in the near future.

From the modeling side, different atmospheric global models have been applied to study the thermospheric temperatures. The Mars Thermospheric General Circulation Model (MTGCM) was the first general circulation model (GCM) able to study the Martian upper atmosphere [*Bougher et al.*, 1999]. The MTGCM is coupled to the NASA-Ames MGCM to account for the effects of the lower atmosphere on the thermosphere, although no downward coupling is enabled. These coupled models have been used to simulate the thermospheric behavior during short periods of time at selected seasons (typically equinox, aphelion, and perihelion) [*Bougher et al.*, 1999, 2000, 2009]. The variability with the solar cycle is studied using different values for the $F_{10.7}$ proxy (the solar radio flux at 10.7 cm, often used as an indication of the overall solar activity level), kept constant during the simulation time [*Bougher et al.*, 2009]. A good agreement with the solar cycle variability of temperatures provided by MGS drag data is achieved when a heating efficiency at the low edge of the experimental values is used [*Bougher et al.*, 2009]. The coupled MGCM-MTGCM has also been validated against SPICAM temperature measurements [*McDunn et al.*, 2010]: two important outcomes of this comparison are, first, the importance of using an appropriate dust distribution to reproduce the observed density and temperature in the mesosphere and, second, that even when using the best available dust scenario, the coupled models predict a mesopause too high and warm when compared to SPICAM data. The effects of varying dust load in the lower atmosphere have also been studied with this model with a focus on the polar warming feature [*Bell et al.*, 2007]; a major finding is that a modification of the dust vertical distribution or the dust column opacity greatly modifies the simulated thermospheric polar warming during solstices. Also, the MTGCM has been coupled to an exospheric model in order to study the effect of the simulated thermospheric variability over the escape rate [*Valeille et al.*, 2009a, 2009b, 2010].

Other Martian global models covering the upper atmosphere have been developed in the last decade. The Mars GCM developed at the Laboratoire de Météorologie Dynamique (LMD-MGCM) [*Forget et al.*, 1999; *Angelats i Coll et al.*, 2005; *González-Galindo et al.*, 2009a, 2013] is the first Mars GCM able to self-consistently simulate the full atmospheric range from the surface to the exobase. The LMD-MGCM has been previously run during a full Martian year to study the seasonal and geographical variability of the thermospheric temperatures [*González-Galindo et al.*, 2009a]. However, the solar activity was kept constant during the whole simulated year, which is obviously far from reality. Similar to the MTGCM, the LMD-MGCM has also been coupled to an exospheric model [*Yagi et al.*, 2012; *Chaufray et al.*, 2015], finding a strong influence of the seasonal and geographical variability of the thermospheric temperatures over the escape rates.

The Martian GCM developed at the Max Planck Institute has also been used recently to simulate the variability of the upper atmosphere during a full Martian year, maintaining a constant solar flux during the simulated year [*Medvedev et al.*, 2013]. The impact of major dust storms on the Martian thermosphere was modeled, showing that momentum transfer by gravity waves is influenced by different dust scenarios. This model has also shown the substantial dynamical and thermal influences of lower atmospheric gravity waves on the mesosphere and lower thermosphere [*Medvedev et al.*, 2011; *Medvedev and Yiğit*, 2012]. Recently, the key role of gravity waves in facilitating CO_2 cloud formation in the upper atmosphere was also confirmed with this model [*Yiğit et al.*, 2015].

Very recently, a new ground-to-exosphere model, the M-GITM, has been developed at the University of Michigan [*Bougher et al.*, 2015a]. It is based on a terrestrial model, but M-GITM uses physical parameterizations adapted for Mars taken from both the MTGCM and the NASA-Ames MGCM. This new model has been used to simulate thermospheric temperatures using three different solar activities, where the solar activity level was held constant during the entire simulation. A first comparison with measured temperatures shows a good agreement, in particular for aphelion conditions.

In this study, we simulate the variability of the Martian upper atmosphere during eight consecutive Martian years (MY24 to MY31, spanning from July 1998 to July 2013) with a ground-to-exosphere GCM, using for the first time a realistic day-to-day variability of the UV solar flux during that period and a dust climatology based on measurements during the whole period. While our first objective is the quantification of the effects of the 11 year solar cycle over the exospheric temperatures, we also study the effects of the 27 day solar rotation cycle and of the presence of global dust storms in the lower atmosphere.

Several observations have unveiled a diversity of effects of the 27 day solar rotation on the Martian upper atmosphere. The effects on the ionosphere are relatively well known, as different instruments and techniques have identified oscillations in the electronic density with periods consistent with that of the solar rotation [*Breus et al.*, 2004; *Withers and Mendillo*, 2005; *Nielsen et al.*, 2006; *Venkateswara Rao et al.*, 2014]. These oscillations have also been found in simulations with the LMD-MGCM [*González-Galindo et al.*, 2013]. Unfortunately, the lack of continuous observations with a reasonable geographical coverage of the Martian neutral upper atmosphere has hindered a similar characterization of the effects of solar rotation on the neutral atmosphere. The exception is the work by *Forbes et al.* [2006], who used the Mars Global Surveyor Precise Orbit Determination (POD) to derive neutral densities at an altitude of 390 km. They found a close relationship between the 27 day solar rotation and the density variations. They also used a semiempirical model of the Martian atmosphere to derive exospheric temperatures, finding a variation of about 1 K for every two-unit change in the $F_{10.7}$ index, although with a large variability.

Numerous previous works have studied the effects of dust storms on the Martian atmosphere, using observations, purely theoretical considerations, or numerical simulations. *Bougher et al.* [1999] simulated the effects of the regional dust storm that developed during the aerobraking phase of the MGS mission (known as the Noachis storm, on MY23) on the densities at the aerobraking altitudes with the coupled Ames GCM/MTGCM. They found that the model underestimated the effects of the Noachis storm when compared to MGS observations. *Withers and Pratt* [2013] analyzed measurements of different instruments during different dust events to find a strong and quick response of the densities (and also the temperatures) in the upper atmosphere to the presence of regional or global dust storms. *Medvedev et al.* [2013] used a GCM to simulate the effects of the global dust storms of MY25 and MY28. They found an unexpectedly strong response of the thermospheric temperature to these dust events and provided the details of how the underlying dynamical processes and the seasonality of the storm affect the thermosphere.

2. Description of the Model and Inputs

For this study we use the LMD-MGCM, an adaptation to Mars of a previous terrestrial GCM [*Forget et al.*, 1999], extended to simulate the whole atmospheric range from the surface to the exobase (top level at about $2 \cdot 10^{-8}$ Pa, corresponding to roughly 200–300 km, depending on the thermal structure) [*Angelats i Coll et al.*, 2005; *González-Galindo et al.*, 2009a]. We use the latest version of the model, including the improvements described in *González-Galindo et al.* [2013]. Two of these improvements are of special relevance for this work: the first one is the incorporation of an improved parameterization of the CO_2 15 μm cooling, which considers the effects of varying atomic oxygen and produces temperatures in better agreement with SPICAM stellar occultation measurements [*López-Valverde et al.*, 2011]; the second one is the modification of the solar variability scheme in the model, which is now able to handle the observed day-to-day variability of the UV solar flux by using a series of polynomial fits for the photoabsorption coefficients as a function of the solar proxy $E_{10.7}$ [*González-Galindo et al.*, 2013]. We obtain the values of this proxy parameter (the integrated extreme ultraviolet flux from 1 to 105 nm) for each sol (Martian day) from MY24 to MY31 from the Solar Irradiance Platform (SIP) [*Tobiska and Bouwer*, 2006]. The variability of this proxy index from 1995 to 2014 (a period including the simulated Martian years) is shown in Figure 1. It can be seen that for MY24 the solar cycle was approaching solar maximum conditions; MY25 corresponds to the period of maximum solar activity, which contained a sharp increase in 2002; during MY26 the solar activity decreases toward solar average conditions; MY27 – MY29 correspond to the last deep solar minimum period. During MY30, the solar flux starts increasing again, and during MY31 the solar flux continues increasing toward the (modest) maximum of the present solar cycle.

The variability of the dust load in the lower atmosphere is known to have a significant impact on the thermosphere [*Keating et al.*, 1998; *Bell et al.*, 2007; *McDunn et al.*, 2010; *González-Galindo et al.*, 2009b; *Withers and Pratt*, 2013]. Our model uses as an input the column dust optical depth (CDOD). This CDOD is retrieved from TES and the Mars Odyssey instrument THermal EMission Imaging System (THEMIS) nadir observations and
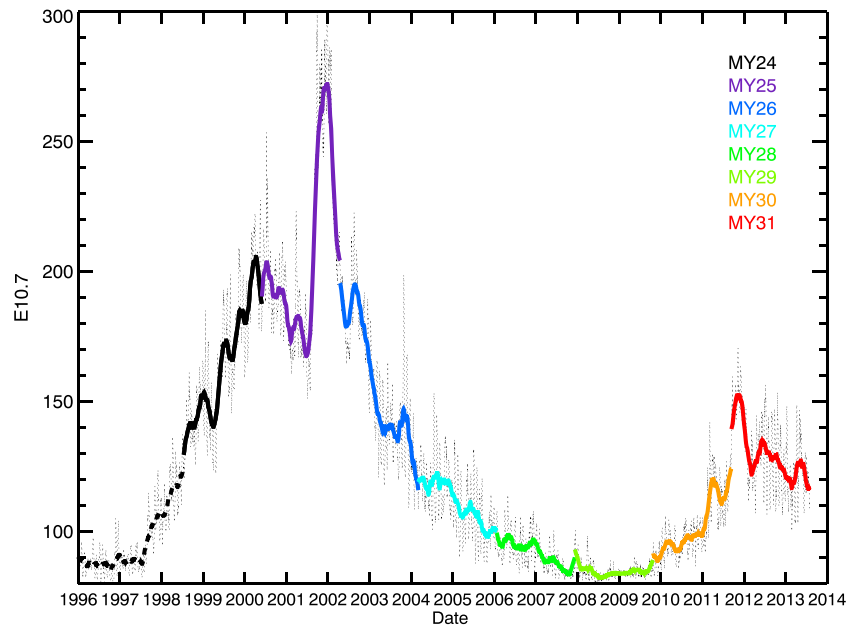
Figure 1. Variation of the solar proxy index $E_{10.7}$ from 1995 to 2014, a period including the simulated Martian years. The thin black dotted line represents the daily value of the $E_{10.7}$ index, while the thick color lines are 81day running mean of the index, with different colors representing the different Martian years being simulated.

estimated from MCS limb observations, after gridding and interpolation to a regular daily map using a combination of "iterative weighted binning" and "kriging" methods [*Montabone et al.*, 2015]. The variability of the CDOD can be seen in the time series at three locations in Figure 13 of *Montabone et al.* [2015], as well as in the zonal means as a function of time and latitude in Figure 21 of the same paper.

The model includes also the radiative effects of water ice clouds, known to have a significant effect over the mesospheric temperatures [*Madeleine et al.*, 2012].

3. Results

In this section we explore the variability of the temperatures in the upper atmosphere predicted by the LMD-MGCM. We will focus on the temperatures at a constant pressure level of 10^{-6} Pa. The temperatures at this pressure level corresponds to exobase temperatures [*González-Galindo et al.*, 2009a]. Our focus is the variability due to the changing solar output and dust load, so we will not address the day-night temperature variability, already studied with the LMD-MGCM [*González-Galindo et al.*, 2009a]. Unless otherwise stated, all the plots below show the zonal mean temperature at constant local time (noon): for every simulated sol, the results at LT = 12 for every grid point are extracted, and a zonal average is applied.

3.1. Validation

Using POD of the MGS spacecraft and a semiempirical atmospheric model, *Forbes et al.* [2008] determined the exospheric density and temperature from February 1999 to July 2005. Due to the characteristics of the MGS orbit, the measurements are strongly biased toward latitudes between 40°S and 60°S during daytime. *Forbes et al.* [2008] proposed a simple fit to the derived exospheric temperature of the form

$$T_{\text{inf}} = 130.7 + 1.53 \cdot \overline{F}_{10.7} - 13.5 \cdot \cos L_s - 85 \tag{1}$$

where T_{inf} is the exospheric temperature and $\overline{F}_{10.7}$ the 81 day running mean of the $F_{10.7}$ solar proxy index.

In Figure 2 we compare the zonal mean exospheric temperatures at noon and at latitude 50°S produced by the model during the eight simulated MYs with the values derived from equation (1) using the daily value of the $\overline{F}_{10.7}$ provided by the Solar Irradiance Platform [*Tobiska et al.*, 2000]. We can see that overall the model matches closely the temperatures derived from *Forbes et al.* [2008]. To quantify the quality of the agreement, we have calculated the normalized root-mean-square difference (NRMSD) between the simulated temperatures and those derived from MGS POD. The value of the NRMSD is of 9.8%, indicating a quite reasonable agreement.
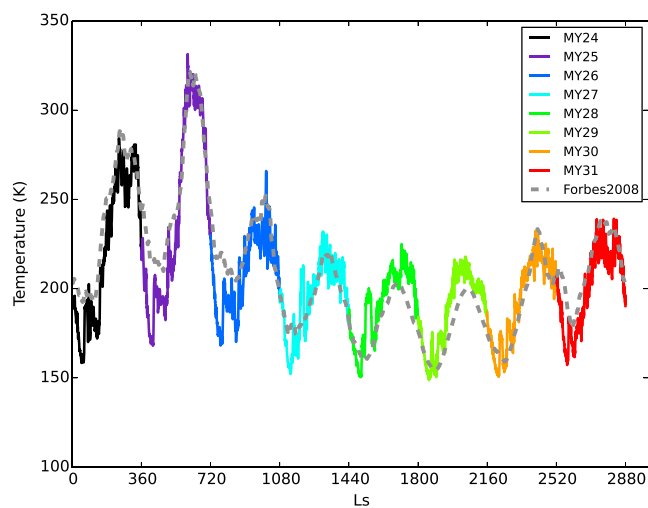
Figure 2. Zonal mean exobase temperatures at noon and latitude = 50°S for the eight simulated MYs, together with the values derived from *Forbes et al.* [2008].

This is in contrast with previous works using the LMD-MGCM [*González-Galindo et al.*, 2009a], where, when using constant values for the $F_{10.7}$ index appropriate for solar minimum, solar average, and solar maximum conditions, the model was found to predict temperatures systematically higher (with an average overestimation of about 20%) than the temperatures derived from POD. The improvement in the comparison is a direct consequence of the improvements introduced into the model and in particular of the improved 15 μm cooling scheme, which produces a stronger cooling in the mesosphere and the lower thermosphere and thus lower thermospheric temperatures. However, there are still differences between the model and the temperatures derived from POD. In particular, during the aphelion season of MY24–MY26 the predicted temperatures are lower than those from *Forbes et al.* [2008]. Also, the temperatures during the perihelion season in the years corresponding to solar minimum conditions are higher in the model. However, a reanalysis of MGS POD densities with a different atmospheric model [*Krasnopolsky*, 2010] suggested that the exospheric temperatures in *Forbes et al.* [2008] during solar minimum conditions might be underestimated. *Krasnopolsky* [2010] also pointed out a possible underestimation of MGS POD densities at the times when the densities are low and thus hard to measure. These corrections to the POD-derived temperatures would bring the model into closer alignment with the observations. MAVEN is already providing model-independent measurements of the exospheric temperatures, together with simultaneous measurements of the EUV solar flux. More meaningful data-model comparisons will be allowed by this new data set.

3.2. Interannual and Solar Cycle Variability

Figure 3 shows the temporal and latitudinal variability of the zonal mean temperatures, as described above, in the period from MY24 to MY31.

The temperatures during each of the different MYs show a similar seasonal pattern, with temperatures increasing from the aphelion season (around $L_s \approx 71$) to the perihelion season ($L_s \approx 251°$), as a result of the high eccentricity of the Martian orbit. Minimum temperatures are predicted for all years at the winter polar night before the aphelion season (between $L_s = 30°$ and $L_s = 60°$ in the southern hemisphere), with temperatures close to 125 K. The cold temperatures in this region exhibit little interannual variability, as expected from the absence of local radiative heating and the little interannual variability of the dust load at this season. Vertical profiles of temperature (not shown) indicate that the cold temperatures affect not only the thermosphere but also the mesosphere. This period of very cold exospheric temperatures in the polar night at aphelion is followed in time by a polar warming with temperatures and durations changing from year to year. It is interesting to note that this polar warming develops at a time where there is not yet illumination in the polar winter region, making its dynamical nature clear. While the thermospheric polar warming is more commonly found during the perihelion season [*Bougher et al.*, 2006], SPICAM stellar occultations [*Forget et al.*, 2009] and electron reflectometry measurements on MGS [*Lillis et al.*, 2008] show signatures of a polar warming during the aphelion season. Different models have been used to study the polar warming in the middle and upper atmosphere, mostly during the perihelion season. *Bell et al.* [2007] showed how the dust load in the lower
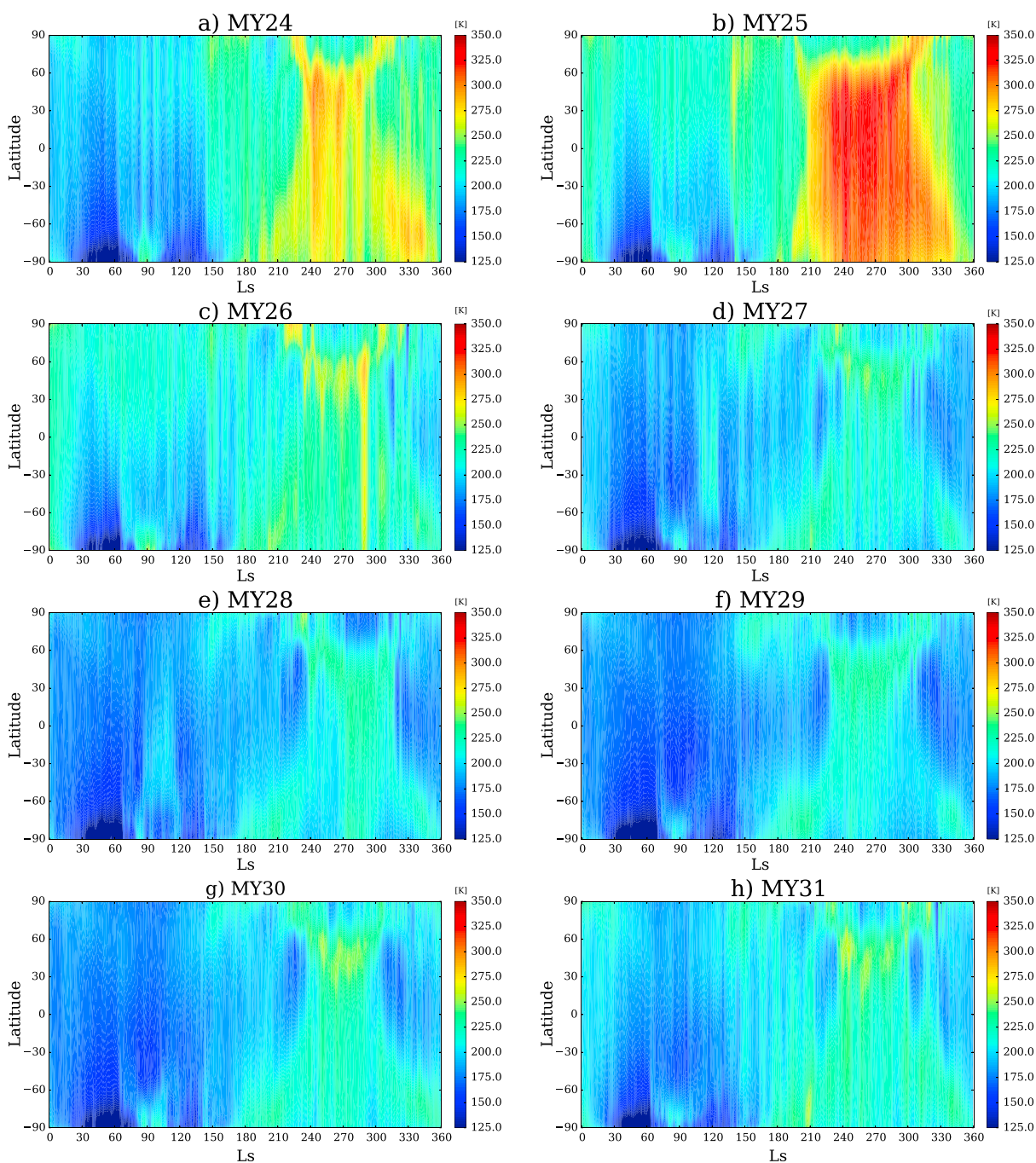
Figure 3. Zonal mean exobase temperatures at noon for (a) MY24, (b) MY25, (c) MY26, (d) MY27, (e) MY28, (f) MY29, (g) MY30, and (h) MY31.

atmosphere affected the intensity of the polar warming. *González-Galindo et al.* [2009b] studied the influence of the in situ thermal tides over the polar warming. *Medvedev et al.* [2011] demonstrated that the dynamical effects of gravity waves lead to an enhancement of both the middle atmosphere and upper atmosphere winter polar warmings. The cold temperatures in the aphelion polar night and the associated polar warming will be studied in more depth in a forthcoming paper.

There are other departures from the temperature distribution expected from radiative considerations only. For example, during the second half of the year the exospheric temperatures exhibit an X-shaped feature in these L_s-latitude maps: the temperatures in the equinox seasons (around $L_s = 180°$ and $L_s = 360°$) are higher in the polar regions than at low latitudes. These maximum temperatures seem to move toward midlatitudes
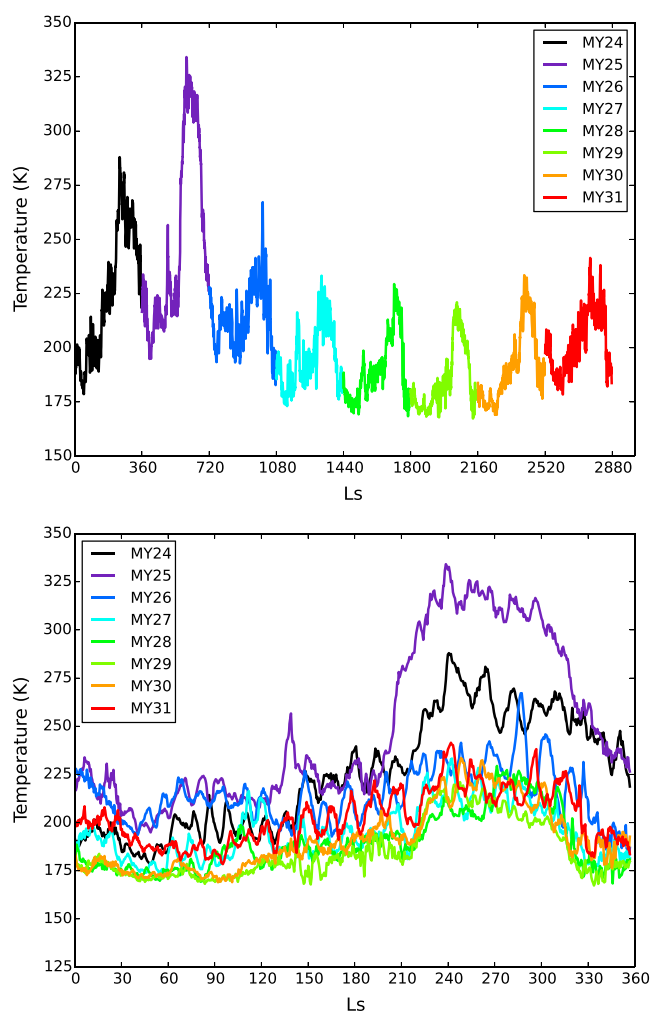
Figure 4. Zonal mean exobase temperatures at the subsolar point for the eight simulated MYs, (top) as a function of eight MYs continuous solar longitude and (bottom) as a function of 360° solar longitude, all years together.

when approaching the solstice season ($L_s = 270°$). The warmest region during perihelion is located at the midlatitudes of the northern (winter) hemisphere. This location far from the subsolar point is, as discussed in previous works [*González-Galindo et al.*, 2009a], another indication of the significant modification of the thermal structure by the general circulation.

The maximum temperatures exhibit a strong interannual variability, ranging from less than 250 K during solar minimum conditions (MY27 to MY30) to more than 325 K for MY25.

The temperature seasonal variability is qualitatively similar to that predicted with a previous version of the LMD-MGCM using a constant solar flux [see *González-Galindo et al.*, 2009a, Figure 1]. Some of the features discussed in the previous paragraph, such as the location of the regions with minimum temperature in the polar night before the aphelion season and the X shape during the second half of the Martian year, were also found in those simulations; i.e., they are a robust feature not significantly affected by variations of the solar flux.

Although all simulated MYs exhibit an aphelion-to-perihelion increase in the global temperature, and especially at low latitudes to midlatitudes, the magnitude of this seasonal contrast presents a significant interannual variability due to the different solar conditions throughout the eight-Martian-year period. This can be better appreciated in Figure 4, where the zonal mean temperatures at the subsolar point are presented. Both the seasonal variability and the effects of the solar cycle can be observed in Figure 4 (top), when compared to Figure 1.

Table 1. Maximum and Minimum Temperatures at the Subsolar Point for Each of the Simulated Martian Years, and the Max-Min Temperature Contrast

MY	T_{min} (K)	T_{max} (K)	ΔT (K)
24	178.7	287.9	109.8
25	194.9	334.1	139.2
26	182.8	267.2	84.8
27	173.1	233.2	60.1
28	168.4	229.4	61.0
29	167.4	221.0	53.6
30	169.1	233.5	64.6
31	178.4	241.4	63.0

When plotting all MYs together (Figure 4, bottom), it reveals that the interannual variability of the temperatures is smaller during the first half of the year, with minimum to maximum values of about 35 K near $L_s = 45°$, 60 K around $L_s = 90°$, and 75 K at $L_s = 150°$. During the second half of the year, these variations can be as large as 150 K around $L_s = 240°$. These large values are the consequence of the particular conditions during MY24 and especially MY25, a year characterized, as we will discuss below in section 3.4.1, both by a strong increase of the solar flux around the perihelion season and by the presence of a global dust storm.

The minimum and maximum temperatures at the subsolar point for each of the simulated Martian years, as well as the seasonal temperature contrast at the subsolar point, are included in Table 1. The seasonal variability of temperatures ranges from around 50–60 K during solar minimum to almost 140 K for MY25. Again, this latter value is affected by the particular conditions during MY25. For comparison, previously published results using a constant solar flux [*González-Galindo et al.*, 2009a] reported a seasonal variability of temperatures at the equator of around 90 K. This result shows the importance of simulating individually each Martian year taking into account the actual dust and solar flux variability within it.

It is worth comparing the temperature variations described above with those recently found using the M-GITM model [*Bougher et al.*, 2015a]. M-GITM predicts a solar cycle variability of exobase temperatures at midafternoon (LT = 15) of 135 K (from 215 K for solar minimum to 350 K for solar maximum conditions) for $L_s = 180$. Both the temperatures and the solar cycle variability at this season are larger in the M-GITM model than in the LMD-MGCM. The aphelion-solar minimum to perihelion-solar maximum temperature contrast is about 200 K for the M-GITM (190 to 390 K), while that for the LMD-MGCM is slightly larger than 150 K (170 to 335 K). The larger temperatures and temperature contrast found by M-GITM seem to indicate that the improved 15 μm cooling parameterization in the LMD-MGCM is more efficient acting as a thermostat. However, other differences, both in the models formulation and in the experimental setup (different specification of dust load and UV solar flux, temperatures obtained at different local times, etc.), may also contribute to the differences. A previous comparison between the LMD-MGCM (using the old 15 μm parameterization) and the MTGCM [*González-Galindo et al.*, 2010] showed that both models predicted similar temperatures when using similar forcings.

3.3. Effects of Solar Rotation

We will focus here on the effects of the 27 day solar rotation cycle on the simulated exospheric temperatures on Mars. These effects can already be seen in Figure 3 as a series of vertical stripes, especially prominent during higher solar activity. To study in more depth these effects, we will concentrate on a particular Martian year, MY24, in which the effects of solar rotation are particularly strong.

In Figure 5 we represent the temporal variability of the temperatures at the subsolar point for MY24 (black line) together with the temporal variability of the $E_{10.7}$ solar proxy index divided by the squared Sun-Mars distance (red line) and of the IR dust opacity (blue line) throughout that year. The most noticeable feature is the strong correlation between the variability of the temperatures and that of the $E_{10.7}$ solar proxy index. The solar rotation with an approximate period of 27 days translates into temperature changes which are in phase with the solar flux change. These oscillations can have peak-to-valley temperature changes as high as 25 K, a similar magnitude to that found by *Forbes et al.* [2006].
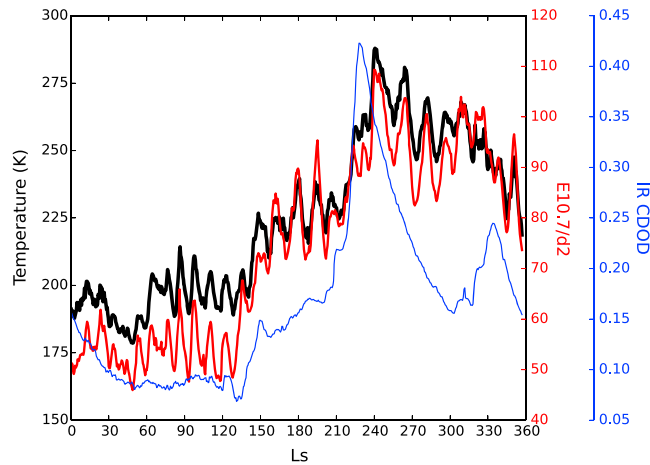
Figure 5. Zonal mean exobase temperatures at the subsolar point for MY24 (black line), variability of the $E_{10.7}$ proxy index during that Martian year (red line), and variability of the CDOD in the IR averaged in the latitude range 30°S–30°N (blue line).

We have performed a spectral decomposition of the zonal mean exobase temperatures at the subsolar point and the $E_{10.7}$ index time series in order to determine correlations between solar and temperature oscillations. Figure 6 shows the normalized power spectra estimated from the full data set for the temperature (black lines) and the $E_{10.7}$ proxy index (red line). Both the temperature and the $E_{10.7}$ power spectra show a prominent signal at periods around 27 days. We have decomposed the exobase temperature full time series following the expression

$$T = T_{res} + \sum_{N=1}^{5} \left[T_N \times \cos[2\pi N(t - p_N)/T_{AO}] \right] + s\bar{E}_{10.7} \qquad (2)$$

where T_N and p_N are the amplitudes and phases of the N wave number oscillation, $T_{AO} = 668.6$ sols and $\bar{E}_{10.7}$ is the 81 day average of $E_{10.7}$. The second term in the right-hand side of equation (2) embeds the seasonal temperature variability considering five harmonics of the Martian year with periods $T = 668.6$, 334.4, 167.2, 83.6, and 41.8 sols. The third term is a high-period solar component, proportional to $\bar{E}_{10.7}$, containing the effect on temperature due to solar flux oscillations with periods larger than 81 days. Therefore, the residual temperature, T_{res}, includes a background temperature and the effect of solar flux low-period (less than 81 days) oscillations. After that decomposition, we have further extracted the best fit harmonic with a quasi-27 day period from T_{res} and the $E_{res} = E_{10.7} - \bar{E}_{10.7}$ time series for each individual MY, thus allowing for an interannual variability of their amplitudes. The average temperature and $E_{10.7}$ index amplitudes of these harmonics are 2.6 K and
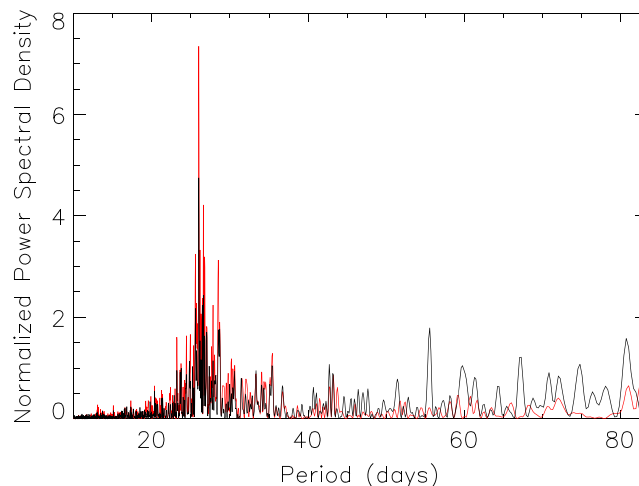

Figure 6. Periodogram of the exospheric temperatures at the subsolar point simulated for MY24 (black line) and of the $E_{10.7}$ proxy solar index for MY24 (red line).
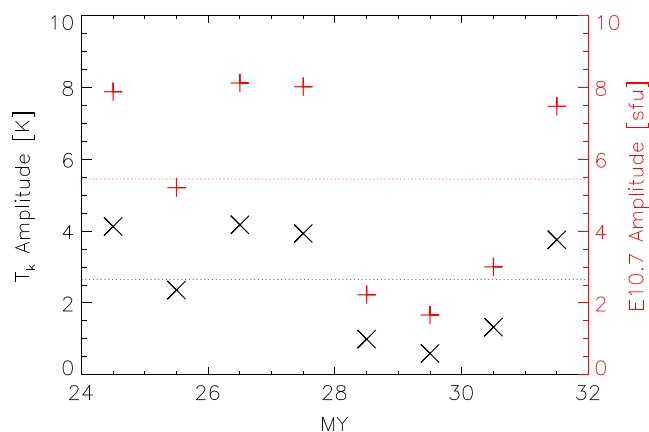
Figure 7. Amplitude of the temperature and solar 27 day oscillations obtained for the eight simulated MYs.

5.4 sfu (solar flux units), respectively. These amplitudes are subject to a significant interannual variability, as can be seen in Figure 7, where we represent the amplitude of the temperature and $E_{10.7}$ 27 day oscillations for each of the simulated MYs. Temperature amplitudes range from less than 1 K during solar minimum to about 4 K. There is a clear correlation between the solar cycle and the amplitudes of the oscillations, with low amplitudes during solar minimum conditions. This behavior agrees with previous analysis of the solar variability, which showed that the amplitude of the solar rotation variability was generally larger during the solar peak than during solar minimum conditions [e.g., *Floyd et al.*, 2002]. However, departures from this overall picture have been found [e.g., *Kane*, 2003]. Interestingly, during MY25, corresponding to solar maximum conditions, the amplitudes (both in the solar flux and in the temperature variabilities) are quite modest. In general, there is a very good correlation between temperature and solar flux 27 day amplitudes, with $\Delta T/\Delta E_{10.7} = 0.544$ K/sfu. Note that this is in reasonable agreement with the value of 0.47 K/sfu derived by *Forbes et al.* [2006]. As a comparison, the average amplitude of the annual and semiannual oscillations obtained from the fit in equation (2) are 21.8 K and 9.5 K, respectively.

3.4. Effects of Global Dust Storms

Among the simulated periods, there are two Martian years characterized by the presence of global dust storms. In particular, during MY25 a global dust storm appeared shortly after $L_s = 180°$, an unusually early time in the dust storm season ($L_s = 180 - 360°$, according to *Kahn et al.* [1992] or *Montabone et al.* [2015]). Dust visible opacities around 4 (for the relationship between IR and visible dust opacities, see *Montabone et al.* [2015]) were reached, and high levels of opacity ($\tau > 2$) were maintained until around $L_s = 230°$, when the dust storm began to settle down. During MY28 a global dust storm took place around $L_s = 270°$, with maximum dust visible opacity around 3.

Here we will focus on the response of the thermosphere to the MY25 and MY28 global dust storms.

3.4.1. MY25 Global Dust Storm

As shown in Figure 8, where the simulated exospheric temperatures at the subsolar point (black line) for MY25, together with the variability of the IR CDOD (blue line) and of the solar activity (red line) are shown, this year is characterized by a strong increase of the solar activity around $L_s = 210°$, almost coincident in time with the onset of the global dust storm around $L_s = 180°$. The temperature at the subsolar point increases sharply by more than 50 K in a few days around $L_s = 210°$, but it is difficult to attribute this temperature increase either to the dust storm, to the solar activity increase, or to a combination of both. In order to separate the effects, we have performed a simulation covering the $L_s = 150 - 360°$ period, using the solar activity for MY25 but the dust scenario of MY24 (purple line). Figure 8 shows the resulting simulated temperatures (gray dashed line). It can be seen that the strong increase of temperature around $L_s = 200°$ is sharper and starts at an earlier time when the dust storm is included in the simulation. There is a significant time lag between the onset of the dust storm and its effects on the exobase at the subsolar point. Temperatures between about $L_s = 200°$ and $L_s = 230°$ remain up to 40 K higher in the simulation with the dust storm. However, after $L_s = 240°$, during the decay phase of the storm, the distribution of the temperature is overall similar in both simulations, showing that the high temperatures predicted after that time are due to the strong increase in solar radiation.
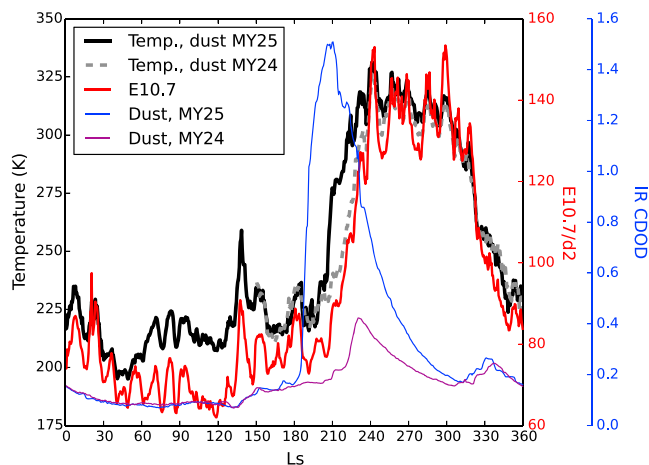
Figure 8. Zonal mean exobase temperatures at the subsolar point for MY25 (black line), zonal mean exobase temperature at the subsolar point when using the solar flux for MY25 but the dust load for MY24, variability of the $E_{10.7}$ proxy index during MY25 (red line), variability of the IR CDOD during MY25 (blue line), and variability of the dust optical depth during MY24 (purple line).

A look at the 2-D latitude-L_s distribution of the temperature effects produced by the dust storm (Figure 9, top) shows that its effect on the exobase temperatures evolves with time. Just after the onset of the dust storm ($L_s = 190$–$200°$), a strong heating is predicted in the polar regions, with the low latitudes alternating periods of weak heatings and coolings (usually less than 15 K). After $L_s \approx 200°$ the atmospheric response changes, showing a strong increase of temperatures (up to ≈ 75 K) at latitudes below 60 and a decrease of the temperatures in the polar regions, in particular in the north (winter) pole. The strongest effect occurs at about $L_s = 220°$, coincident with the peak of the dust storm, and the magnitude of the temperature modification decreases during the decay phase of the storm.
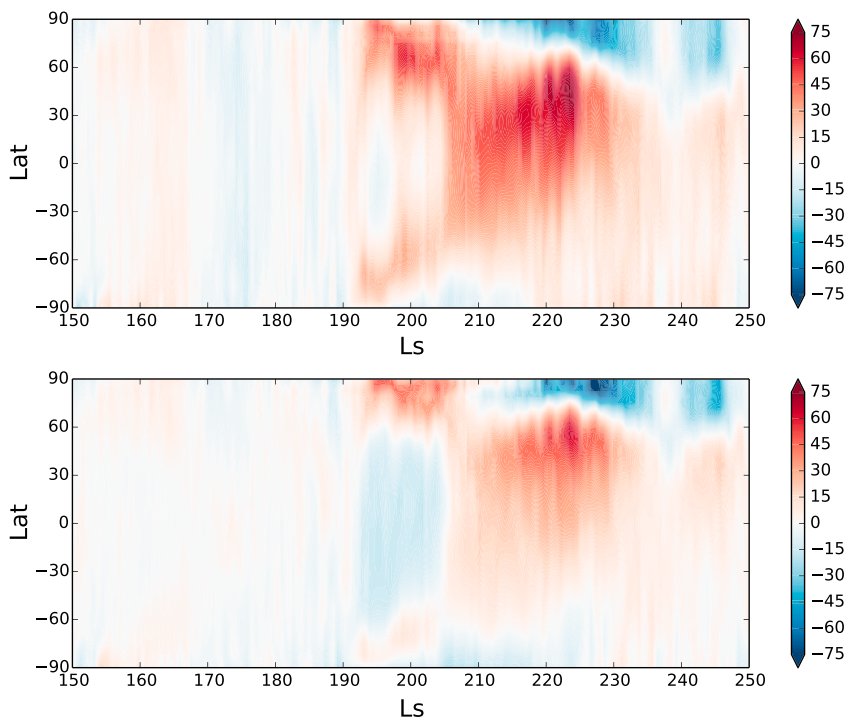

Figure 9. Zonal mean temperature difference between the simulation using the dust load for MY25 and the one with the dust for MY24, as a function of latitude and L_s during the dust storm period. (top) Differences at the 1e−6 Pa pressure level. (bottom) Differences at the 1e−4 Pa pressure level.
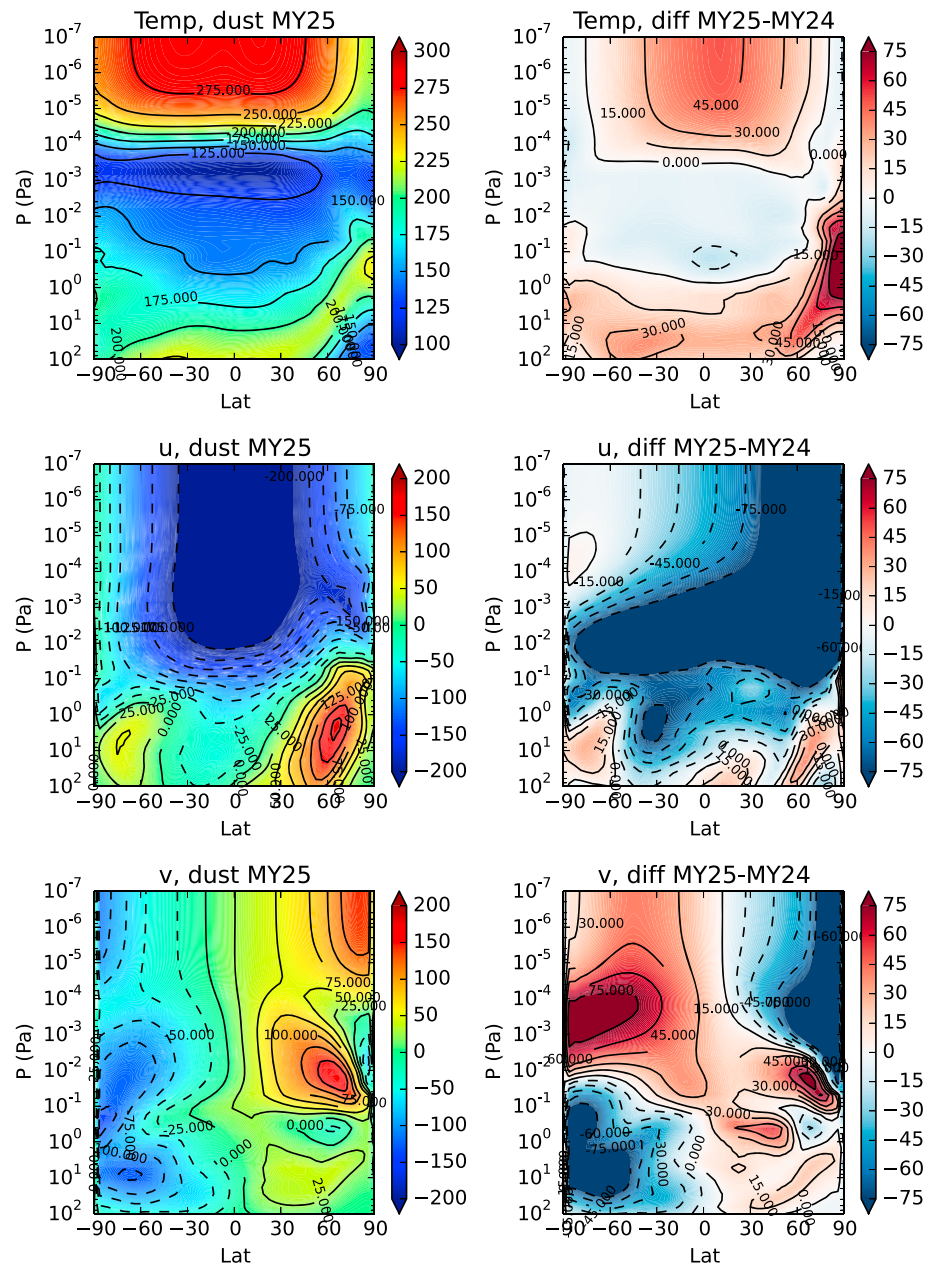
Figure 10. (top row) Zonal mean temperature, (middle row) zonal wind, and (bottom row) meridional wind for the (left column) simulation using the dust load for MY25 and (right column) differences with the simulation using the dust load for MY24, for $L_s = 210°$.

The structure of the temperature field modification in the thermosphere is a consequence of the perturbation of the thermospheric dynamical structure by the dust storm (Figure 10). The strong westward jet predicted by the model at all latitudes in the mesosphere and the thermosphere is strongly reinforced, in particular in the northern hemisphere. The meridional winds are also significantly affected. While below about 0.01 Pa the dominant equator-to-poles transport during the day (due to the subsolar-antisolar circulation) is reinforced, in the upper atmosphere this subsolar-antisolar circulation transport is damped by the development of the dust storm. This modifies the distribution of the adiabatic heating/cooling by the winds, which results in the changes to the thermal structure.

Medvedev et al. [2013] simulated the impact on the temperature and the dynamics of the Martian thermosphere of the MY25 and MY28 dust storms. For the MY25 storm, a decrease of the thermospheric temperatures
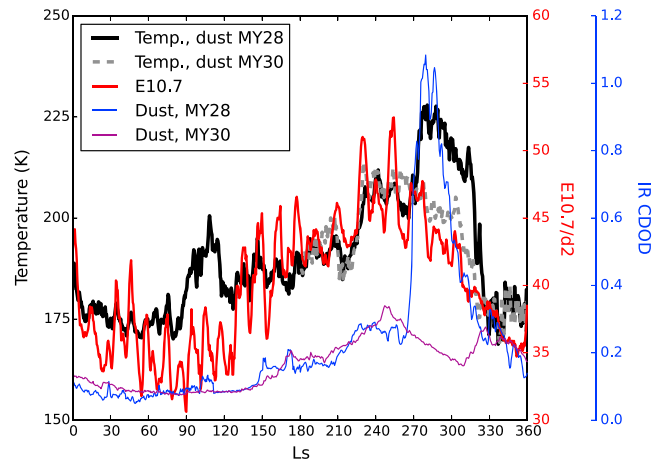
Figure 11. As in Figure 5 but for MY28.

at all latitudes except in the polar region is predicted by the Max Planck Mars GCM. This prediction may seem in contradiction with the warming of the exobase level at all latitudes below 60° found with the LMD-MGCM. However, it has to be taken into account that (i) *Medvedev et al.* [2013] only simulated a period of 10° of L_s after the onset of the storms, that is, $L_s = 190 – 200°$ for the MY25 storm and (ii) the Max Planck model extends up to $3.6 \cdot 10^{-6}$ Pa. When looking at the predictions of the LMD-MGCM in the lower thermosphere (10^{-4} Pa levels, Figure 9, bottom), the response of the LMD-MGCM to the dust storm during the $L_s = 190 – 200°$ period is qualitatively similar to that of the model in *Medvedev et al.* [2013]: the temperatures increase in the poles and decrease in the low latitudes.

3.4.2. MY28 Global Dust Storm

Figure 11 is similar to Figure 8, but it represents the results for MY28. In this case it can clearly be seen that the development of the dust storm around $L_s = 270°$ coincides with a significant increase of the temperature at the exobase. This increase is not simultaneous to any strong increase in the solar activity, as it was the case in the MY25 case. A comparison with a simulation covering the $L_s = 180 – 360°$ period using the solar flux for MY28 but the dust load for MY30 (gray line in Figure 11) indicates that the dust storm produces an increase of temperature of about 25 K in the $L_s = 270 – 330°$ period.

A look at the latitude-L_s structure of the temperature difference between both simulations (Figure 12) shows that the effect of the dust storm at $L_s = 270°$ is an increase of temperatures at all latitudes, except in the high latitudes of the northern hemisphere, where the temperature decreases. In this case, the response of the modeled thermosphere to the dust storm in MY28 is similar to that in *Medvedev et al.* [2013]. The response in the lower thermosphere (figure not shown) shows no significant difference with that at the 10^{-6} Pa level.

It has to be taken into account that the LMD-MGCM and the Max Planck Mars GCM present significant differences. Among those most relevant for the description of the upper atmosphere are (i) the Max Planck Mars
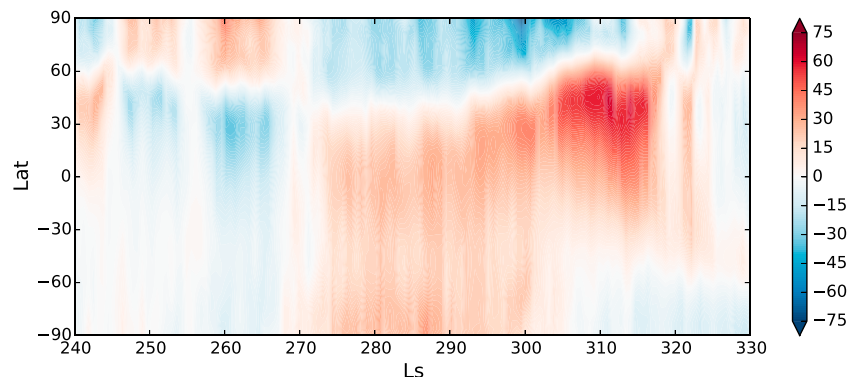

Figure 12. Zonal mean temperature difference, at the 10^{-6} Pa level, between the simulation using the dust load for MY28 and the one with the dust for MY30, as a function of latitude and L_s during the dust storm period.

GCM takes into account the direct propagation and dissipation of nonorographic gravity waves created in the lower atmosphere, based on the gravity wave scheme of *Yiğit et al.* [2008], while the LMD-MGCM only includes a parameterization of the effects of orographic gravity waves and (ii) the LMD-MGCM includes the effects of the atomic oxygen variability due to photochemistry, diffusion, and transport in the 15 μm cooling scheme, while the Max Planck Mars GCM uses a fixed and constant atomic oxygen profile. A recent comparison between both models [*Medvedev et al.*, 2015], as well as previous works [*Forget et al.*, 2009; *Medvedev et al.*, 2011; *Medvedev and Yiğit*, 2012], have underlined how both factors affect the thermal and dynamical structure of the upper atmosphere. Even more, strong feedback are expected during dust storm seasons. So *Medvedev et al.* [2013] show how the dust storms modulate the general circulation of the atmosphere, which then influences the propagation and dissipation characteristics of gravity waves, which in turn impact back the dynamics. A change in the atomic oxygen distribution during a dust storm, due to the modification of the thermal and dynamical structure of the atmosphere, is also to be expected, which can influence back the temperature distribution through a modification of the 15 μm cooling. In spite of these differences, both models predict a similar strong response to the global dust storms. This indicates that this response is a robust, model-independent feature.

4. Summary and Conclusions

We have simulated with the LMD-MGCM, a ground-to-exosphere global climate model for Mars, the variability of the dayside temperatures in the upper thermosphere during eight Martian years (MY24–31, corresponding to the 1998–2013 period). To our knowledge, this is the first time that such a long period has been simulated with a Martian global model using the observed day-to-day variability of the UV solar flux and of the atmospheric dust load. The following conclusions are obtained from our results:

1. The simulated temperatures are in good agreement with those derived from Precise Orbit Determination of MGS spacecraft [*Forbes et al.*, 2008].
2. The aphelion-to-perihelion seasonal temperature variation is a persistent feature in our simulations, but its intensity is strongly affected by the solar cycle. This temperature variation ranges from 50 K during the years corresponding to the latest deep solar minimum to about 140 K for MY25, corresponding to solar maximum conditions.
3. A significant interannual variability of the temperatures, due to both the 11 year solar cycle and the variability of the dust load in the lower atmosphere, is predicted by our model. This variability is weaker during the first half of the year (about 35 K for L_s around 45°) and stronger close to perihelion (approximately 150 K at $L_s = 240°$).
4. The variation in the solar output produced by the 27 day solar rotation cycle is seen in the simulated exobase temperatures. The average amplitude of this oscillation is of about 2.5 K for the MY24–MY31 period, but with important interannual variability, reaching about 4 K for some of the simulated years.
5. The global dust storms in MY25 and MY28 significantly impact the temperatures at the exobase. In general, a warming at low latitudes and midlatitudes and a cooling at high latitudes is the main effect of both storms. This response is qualitatively similar to that previously found with the Max Planck Mars GCM [*Medvedev et al.*, 2013]. However, the atmospheric response to the storm changes with time and is different at different altitudes within the thermosphere.

We conclude that the inclusion of the variability of the two major forcings of the Martian upper atmosphere, the solar UV radiation, and the dust load in the lower atmosphere, is essential to properly simulate the thermospheric temperatures. Given that these temperatures are a key driver of most processes producing atmospheric escape, we can anticipate a significant effect of the solar and dust variability on the escape rate, with important implications for the interpretation of present-day measurements of the escape rate and for the long-term evolution of the upper atmosphere. The variability of the simulated escape rates will be the subject of a forthcoming paper.

Due to the lack of continuous coverage of the Martian thermosphere to date, some of the predictions of our model remain to be confirmed. For example, the effects of solar rotation over the ionospheric densities have been studied, but the impact on the thermospheric temperatures have been only indirectly deduced [*Forbes et al.*, 2006]. Another interesting prediction of the model is the presence of very cold temperatures (around 150 K and only weakly affected by interannual variability) at the exobase during the polar winter in the southern hemisphere, a period followed by the presence of relatively short thermospheric polar warmings

in this region. The MAVEN mission, already operating on Martian orbit and producing its first results [e.g., *Bougher et al.*, 2015b], offers a great opportunity to confirm or reject these predictions and suggest directions in which to improve the model in the near future. For example, the model does not account for the effects of nonorographic small-scale gravity waves, known to affect the thermal and dynamical structure of the upper atmosphere [e.g., *Medvedev et al.*, 2011; *Medvedev and Yiğit*, 2012; *Medvedev et al.*, 2015; *Yiğit et al.*, 2015]. In particular, it is known that, on the Earth, gravity waves significantly cool down the exobase [*Yiğit and Medvedev*, 2009] and that solar flux variations affect gravity wave propagation [*Yiğit and Medvedev*, 2010]. The results presented here can be modified by these effects.

References

Angelats i Coll, M., F. Forget, M. A. López-Valverde, and F. González-Galindo (2005), The first Mars thermospheric general circulation model: The Martian atmosphere from the ground to 240 km, *Geophys. Res. Lett.*, *32*, L04201, doi:10.1029/2004GL021368.

Bell, J. M., S. W. Bougher, and J. R. Murphy (2007), Vertical dust mixing and the interannual variations in the Mars thermosphere, *J. Geophys. Res.*, *112*, E12002, doi:10.1029/2006JE002856.

Bougher, S., A. Brain, J. Fox, F. González-Galindo, C. Simon-Wedlund, and P. Withers (2015), Upper atmosphere and ionosphere, in *Mars II*, edited by B. Haberle et al., Cambridge Univ. Press, Cambridge, U. K.

Bougher, S. W., S. Engel, R. G. Roble, and B. Foster (1999), Comparative terrestrial planet thermospheres 2. Solar cycle variation of global structure and winds at equinox, *J. Geophys. Res.*, *104*, 16,591–16,611, doi:10.1029/1998JE001019.

Bougher, S. W., S. Engel, R. G. Roble, and B. Foster (2000), Comparative terrestrial planet thermospheres 3. Solar cycle variation of global structure and winds at solstices, *J. Geophys. Res.*, *105*, 17,669–17,692, doi:10.1029/1999JE001232.

Bougher, S. W., J. M. Bell, J. R. Murphy, M. A. Lopez-Valverde, and P. G. Withers (2006), Polar warming in the Mars thermosphere: Seasonal variations owing to changing insolation and dust distributions, *Geophys. Res. Lett.*, *33*, L02203, doi:10.1029/2005GL024059.

Bougher, S. W., T. M. McDunn, K. A. Zoldak, and J. M. Forbes (2009), Solar cycle variability of Mars dayside exospheric temperatures: Model evaluation of underlying thermal balances, *Geophys. Res. Lett.*, *36*, L05201, doi:10.1029/2008GL036376.

Bougher, S. W., D. Pawlowski, J. M. Bell, S. Nelli, T. McDunn, J. R. Murphy, M. Chizek, and A. Ridley (2015a), Mars Global Ionosphere-Thermosphere Model: Solar cycle, seasonal, and diurnal variations of the Mars upper atmosphere, *J. Geophys. Res. Planets*, *120*, 311–342, doi:10.1002/2014JE004715.

Bougher, S. W., R. H. Tolson, P. R. Mahaffy, T. E. Johnston, K. Olsen, and J. M. Bell (2015b), *Trends in Mars Thermospheric Density and Temperature Structure Obtained From MAVEN In-Situ Datasets: Interpretation Using Global Models*, vol. 1, 20903 pp., Joint Am. Astron. Soc./AGU Triennial Earth Sun Summit, held in Indianapolis, 26–30 April.

Breus, T. K., A. M. Krymskii, D. H. Crider, N. F. Ness, D. Hinson, and K. K. Barashyan (2004), Effect of the solar radiation in the topside atmosphere/ionosphere of Mars: Mars Global Surveyor observations, *J. Geophys. Res.*, *109*, A09310, doi:10.1029/2004JA010431.

Chaufray, J.-Y., F. Gonzalez-Galindo, F. Forget, M. A. Lopez-Valverde, F. Leblanc, R. Modolo, and S. Hess (2015), Variability of the hydrogen in the Martian upper atmosphere as simulated by a 3D atmosphere-exosphere coupling, *Icarus*, *245*, 282–294, doi:10.1016/j.icarus.2014.08.038.

Floyd, L., W. K. Tobiska, and R. P. Cebula (2002), Solar UV irradiance, its variation, and its relevance to the Earth, *Adv. Space Res.*, *29*, 1427–1440, doi:10.1016/S0273-1177(02)00202-8.

Forbes, J. M., S. Bruinsma, and F. G. Lemoine (2006), Solar rotation effects on the thermospheres of Mars and Earth, *Science*, *312*, 1366–1368.

Forbes, J. M., F. G. Lemoine, S. L. Bruinsma, M. D. Smith, and X. Zhang (2008), Solar flux variability of Mars' exosphere densities and temperatures, *Geophys. Res. Lett.*, *35*, L01201, doi:10.1029/2007GL031904.

Forget, F., F. Hourdin, R. Fournier, C. Hourdin, O. Talagrand, M. Collins, S. R. Lewis, P. L. Read, and J.-P. Huot (1999), Improved general circulation models of the Martian atmosphere from the surface to above 80 km, *J. Geophys. Res.*, *104*, 24,155–24,176.

Forget, F., F. Montmessin, J.-L. Bertaux, F. González-Galindo, S. Lebonnois, E. Quémerais, A. Reberac, E. Dimarellis, and M. A. López-Valverde (2009), Density and temperatures of the upper Martian atmosphere measured by stellar occultations with Mars Express SPICAM, *J. Geophys. Res.*, *114*, E01004, doi:10.1029/2008JE003086.

González-Galindo, F., F. Forget, M. A. López-Valverde, M. Angelats i Coll, and E. Millour (2009a), A ground-to-exosphere Martian general circulation model: 1. Seasonal, diurnal, and solar cycle variation of thermospheric temperatures, *J. Geophys. Res.*, *114*, E04001, doi:10.1029/2008JE003246.

González-Galindo, F., F. Forget, M. A. López-Valverde, and M. Angelats i Coll (2009b), A ground-to-exosphere Martian general circulation model: 2. Atmosphere during solstice conditions. Thermospheric polar warming, *J. Geophys. Res.*, *114*, E08004, doi:10.1029/2008JE003277.

González-Galindo, F., S. W. Bougher, M. A. López-Valverde, F. Forget, and J. Murphy (2010), Thermal and wind structure of the Martian thermosphere as given by two general circulation models, *Planet. Space Sci.*, *58*, 1832–1849, doi:10.1016/j.pss.2010.08.013.

González-Galindo, F., J. Y. Chaufray, M. A. Lopez-Valderde, G. Gilli, F. Leblanc, R. Modolo, S. Hess, and M. Yagi (2013), 3D Martian ionosphere model: I. The photochemical ionosphere below 180 km, *J. Geophys. Res. Planets*, *118*, 2105–2123, doi:10.1002/jgre.20150.

Kahn, R. A., T. Z. Martin, and R. W. Zurek (1992), The Martian dust cycle, in *Mars*, pp. 1017–1053, Univ. of Arizona Press, Tucson, Ariz.

Kane, R. P. (2003), Fluctuations in the ∼27-day sequences in the solar index F10 during solar cycles 22–23, *J. Atmos. Sol. Terr. Phys.*, *65*, 1169–1174, doi:10.1016/S1364-6826(03)00167-6.

Keating, G. M., et al. (1998), The structure of the upper atmosphere of Mars: In situ accelerometer measurements from Mars Global Surveyor, *Science*, *279*, 1672–1676, doi:10.1126/science.279.5357.1672.

Keating, G. M., S. W. Bougher, J. M. Forbes, M. E. Theriot, and R. H. Tolson (2009), The Mars thermosphere and exosphere climatology from accelerometer experiment measurements, in *European Planetary Science Congress*, vol. 2009, 664 pp., held in Potsdam, Germany, 14–18 Sept.

Krasnopolsky, V. A. (2010), Solar activity variations of thermospheric temperatures on Mars and a problem of {CO} in the lower atmosphere, *Icarus*, *207*, 638–647, doi:10.1016/j.icarus.2009.12.036.

Lillis, R. J., S. W. Bougher, D. L. Mitchell, D. a. Brain, R. P. Lin, and M. H. Acuña (2008), Continuous monitoring of nightside upper thermospheric mass densities in the Martian southern hemisphere over 4 Martian years using electron reflectometry, *Icarus*, *194*, 562–574, doi:10.1016/j.icarus.2007.09.031.

López-Valverde, M. A., F. González-Galindo, and M. López-Puertas (2011), Revisiting the radiative balance of the mesosphere of Mars, in *Mars Atmosphere: Modelling and Observation*, edited by F. Forget and E. Millour, pp. 359–362, held in Paris, France, 8–11 Feb.

Madeleine, J.-B., F. Forget, E. Millour, T. Navarro, and A. Spiga (2012), The influence of radiatively active water ice clouds on the Martian climate, *Geophys. Res. Lett.*, *39*, L23202, doi:10.1029/2012GL053564.

McCleese, D. J., et al. (2010), Structure and dynamics of the Martian lower and middle atmosphere as observed by the Mars Climate Sounder: Seasonal variations in zonal mean temperature, dust, and water ice aerosols, *J. Geophys. Res.*, *115*, E12016, doi:10.1029/2010JE003677.

McDunn, T. L., S. W. Bougher, J. Murphy, M. D. Smith, F. Forget, J.-L. Bertaux, and F. Montmessin (2010), Simulating the density and thermal structure of the middle atmosphere (80–130 km) of Mars using the MGCM-MTGCM: A comparison with MEX/SPICAM observations, *Icarus*, *206*, 5–17, doi:10.1016/j.icarus.2009.06.034.

Medvedev, A. S., and E. Yiğit (2012), Thermal effects of internal gravity waves in the Martian upper atmosphere, *Geophys. Res. Lett.*, *39*, L05201, doi:10.1029/2012GL050852.

Medvedev, A. S., E. Yiğit, P. Hartogh, and E. Becker (2011), Influence of gravity waves on the Martian atmosphere: General circulation modeling, *J. Geophys. Res.*, *116*, E10004, doi:10.1029/2011JE003848.

Medvedev, A. S., E. Yiğit, T. Kuroda, and P. Hartogh (2013), General circulation modeling of the Martian upper atmosphere during global dust storms, *J. Geophys. Res. Planets*, *118*, 2234–2246, doi:10.1002/2013JE004429.

Medvedev, A. S., F. González-Galindo, E. Yiğit, A. G. Feofilov, F. Forget, and P. Hartogh (2015), Cooling of the Martian thermosphere by CO_2 radiation and gravity waves: An intercomparison study with two general circulation models, *J. Geophys. Res. Planets*, *120*, 913–927, doi:10.1002/2015JE004802.

Montabone, L., F. Forget, E. Millour, R. Wilson, S. Lewis, B. Cantor, D. Kass, A. Kleinböehl, M. Lemmon, M. Smith, and M. Wolff (2015), Eight-year climatology of dust optical depth on Mars, *Icarus*, *251*, 65–95, doi:10.1016/j.icarus.2014.12.034.

Nielsen, E., H. Zou, D. A. Gurnett, D. L. Kirchner, D. D. Morgan, R. Huff, R. Orosei, A. Safaeinili, J. J. Plaut, and G. Picardi (2006), Observations of vertical reflections from the topside Martian ionosphere, *Space Sci. Rev.*, *126*, 373–388, doi:10.1007/s11214-006-9113-y.

Smith, M. D. (2004), Interannual variability in tes atmospheric observations of Mars during 1999–2003, *Icarus*, *167*, 148–165.

Tobiska, W. K., and S. D. Bouwer (2006), New developments in SOLAR2000 for space research and operations, *Adv. Space Res.*, *37*, 347–358, doi:10.1016/j.asr.2005.08.015.

Tobiska, W. K., T. Woods, F. Eparvier, R. Viereck, L. Floyd, D. Bouwer, G. Rottman, and O. R. White (2000), The SOLAR2000 empirical solar irradiance model and forecast tool, *J. Atmos. Sol. Terr. Phys.*, *62*, 1233–1250.

Valeille, A., V. Tenishev, S. W. Bougher, M. R. Combi, and A. F. Nagy (2009a), Three-dimensional study of Mars upper thermosphere/ionosphere and hot oxygen corona: 1. General description and results at equinox for solar low conditions, *J. Geophys. Res.*, *114*, E11005, doi:10.1029/2009JE003388.

Valeille, A., M. R. Combi, S. W. Bougher, V. Tenishev, and A. F. Nagy (2009b), Three-dimensional study of Mars upper thermosphere/ionosphere and hot oxygen corona: 2. Solar cycle, seasonal variations, and evolution over history, *J. Geophys. Res.*, *114*, E11006, doi:10.1029/2009JE003389.

Valeille, A., S. W. Bougher, V. Tenishev, M. R. Combi, and A. F. Nagy (2010), Water loss and evolution of the upper atmosphere and exosphere over Martian history, *Icarus*, *206*, 28–39, doi:10.1016/j.icarus.2009.04.036.

Venkateswara Rao, N., N. Balan, and A. K. Patra (2014), Solar rotation effects on the Martian ionosphere, *J. Geophys. Res. Space Physics*, *119*, 6612–6622, doi:10.1002/2014JA019894.

Withers, P., and M. Mendillo (2005), Response of peak electron densities in the Martian ionosphere to day-to-day changes in solar flux due to solar rotation, *Planet. Space Sci.*, *53*, 1401–1418, doi:10.1016/j.pss.2005.07.010.

Withers, P., and R. Pratt (2013), An observational study of the response of the upper atmosphere of Mars to lower atmospheric dust storms, *Icarus*, *225*, 378–389, doi:10.1016/j.icarus.2013.02.032.

Yagi, M., F. Leblanc, J. Y. Chaufray, F. Gonzalez-Galindo, S. Hess, and R. Modolo (2012), Mars exospheric thermal and non-thermal components: Seasonal and local variations, *Icarus*, *221*, 682–693, doi:10.1016/j.icarus.2012.07.022.

Yiğit, E., and A. S. Medvedev (2009), Heating and cooling of the thermosphere by internal gravity waves, *Geophys. Res. Lett.*, *36*, L14807, doi:10.1029/2009GL038507.

Yiğit, E., and A. S. Medvedev (2010), Internal gravity waves in the thermosphere during low and high solar activity: Simulation study, *J. Geophys. Res.*, *115*, A00G02, doi:10.1029/2009JA015106.

Yiğit, E., A. D. Aylward, and A. S. Medvedev (2008), Parameterization of the effects of vertically propagating gravity waves for thermosphere general circulation models: Sensitivity study, *J. Geophys. Res.*, *113*, D19106, doi:10.1029/2008JD010135.

Yiğit, E., A. S. Medvedev, and P. Hartogh (2015), Gravity waves and high-altitude CO_2 ice cloud formation in the Martian atmosphere, *Geophys. Res. Lett.*, *42*, 4294–4300, doi:10.1002/2015GL064275.